Solar Physics
DOI: 10.1007/●●●●●-●●●-●●●-●●●●-●

Hydrodynamic aspects of solar wind and coronal mass ejection expansion and evolution investigated with Space-weather Utilities for Research and Forecasting (SURF).

Mathew J. Owens[1] · **Luke A. Barnard**[1]

Abstract We introduce Space-weather Utilities for Research and Forecasting (SURF), a flexible modelling framework for reconstructing and forecasting large-scale solar wind structure. SURF incorporates both the established incompressible "HUXt" model and a newly developed one-dimensional, compressible hydrodynamic solver ("hydro"). The new solver relaxes the incompressibility assumption while retaining the computational efficiency required for ensemble forecasting, uncertainty quantification, and large parametric studies. SURF-hydro solves the 1D Euler equations in spherical geometry using finite-volume methods with Riemann solvers and second-order spatial reconstruction. It is shown to accurately reproduce the analytical "Parker nozzle" pressure-driven expansion solution to a uniform spherically expanding solar wind, demonstrating adequate numerical fidelity. Using 30 years of near-Earth OMNI observations, we derive empirical relations between speed, density, and temperature at 1 AU and map these back to 0.1 AU to provide non-equilibrium boundary conditions for SURF-hydro. This approach reproduces realistic solar wind speed, density and temperature variability at 1 AU and performs favourably compared to operational WSA–Enlil simulations which are based on equilibrium thermodynamic relations at 0.1 AU. SURF-hydro is also shown to reproduce the key features of coronal mass ejection (CME) expansion and evolution, enabling rapid exploration of CME parameter space. For one particular realisation of a structured solar wind, sensitivity tests demonstrate that CME density and temperature at 0.1 AU can alter 1 AU transit times and arrival speeds by 15–20%, highlighting an under-explored source of forecast uncertainty. SURF-hydro therefore provides a computationally efficient bridge between idealised models and full 3D magnetohydrodynamic simulations, enabling systematic investigation of boundary

✉ M.J. Owens
m.j.owens@reading.ac.uk

[1] Department of Meteorology, University of Reading, Earley Gate, PO Box 243, Reading RG6 6BB, UK

condition assumptions and CME parameter sensitivity for both research and operational space-weather forecasting.

1. Introduction

Reconstruction of the large-scale solar wind state underpins a huge range of scientific and space weather forecasting applications. The standard methodology is to combine individual coronal and solar wind (or heliospheric) models, typically with an interface around 0.1 AU, where the solar wind flow is already super-magnetosonic. There are now a wide range of three dimensional magnetohydrodyanmic (3DMHD) solar wind models, such as Enlil (Odstrcil and Pizzo 1999), EUHFORIA (Pomoell and Poedts 2018), SWMF (Toth et al. 2005), SUSANOO (Shiota and Kataoka 2016), HelioMAS (Riley, Linker, and Mikic 2001), ICARUS (Baratashvili et al. 2025) and GAMERA (Merkin et al. 2016). These models accurately capture the large-scale dynamics of a magnetised fluid flow. But there are many situations – such as large ensembles of runs for uncertainty quantification (Owens and Riley 2017) and data assimilation (Barnard et al. 2020), large-scale parametric studies (**?**), long-duration runs for planetary studies (O'Donoghue et al. 2025), adjoint models for data assimilation (Lang and Owens 2019) – where the computational expense and code complexity of 3DMHD becomes prohibitive. In such situations it is useful to sacrifice a small amount of physical fidelity for greatly increased computational efficiency. Highly idealised models can be both extremely rapid and useful, particularly for forecasting (e.g. Hinterreiter et al. 2021). But there is also a middle ground, using what is best referred to as a "reduced-physics" approximation. The heliospheric upwind extrapolation model with time dependence (HUXt; Owens et al. 2020; Barnard and Owens 2022) is one such reduced-physics model that has found use for both forecasting (https://swxforecastlab.org/forecasts.html) and science (e.g. Watson et al. 2025).

HUXt treats the solar wind as a one dimensional, incompressible hydrodyanmic flow. The 1D approximation is well justified; the solar wind flow is observed to be highly radial in most situations (e.g. Scherer et al. 2001; Owens and Cargill 2004), and even complex three dimensional structures like coronal mass ejections (CMEs) behave as quasi-one-dimensional structures, at least to first order, owing to their rapid spherical expansion (Owens, Lockwood, and Barnard 2017). The hydrodyanmic approximation can also be justified with simple order-of-magnitude arguments, with the 1-AU solar wind displaying dynamic flow pressure around two orders of magnitude higher than either the thermal or magnetic pressures. The incompressible assumption is perhaps the hardest to justify. While HUXt has been shown to produce flow fields in very close agreement ($\sim 5\%$) to 3DMHD for the same boundary conditions (Owens et al. 2020), we here seek to relax the incompressible approximation by introducing a compressible hydrodyanmic solver – "hydro" – that does not sacrifice too much of the computationally efficiency that makes HUXt a useful forecast and research tool.

A significant amount of open-source supporting infrastructure has been built up around the HUXt model. The HUXt codebase now contains easy-to-use

capability for driving HUXt with semi-empirical (Arge et al. 2003), and full MHD (Linker et al. 1999) coronal model output, as well as from coronal tomography (Bunting et al. 2024) and cone-model CMEs (Zhao, Plunkett, and Liu 2002), and boundary conditions derived directly from in situ observations (Owens et al. 2026). Support exists for both inner heliosphere ensemble (Owens and Riley 2017) and outer heliosphere science (O'Donoghue et al. 2025), and for both steady-state and time-dependent (Owens, Barnard, and Arge 2024) ambient solar wind. HUXt can readily be run in 1-, 2- or 3-dimensions, with field-line tracing, time series and CME arrival times at any specified body Using, and with an array of visualisation options. We seek to exploit this framework for the new hydro model and other future developments. For this reason, we refer to the general modelling framework as SURF: Space-weather Utilities for Research and Forecasting. HUXt and hydro are modelling options within SURF.

Section 2 outlines the physical equations we seek to solve with the new 'SURF-hydro' model, while Section 3 describes the numerical implementation. Section 4 outlines the analytical 'Parker nozzle' model of a spherically expanding fluid which we use to validate the numerical SURF-hydro solutions. The results are split across two sections: Section 5 details how the ambient solar wind boundary conditions are determined and the resulting model solutions at 1 AU, whereas Section 6. Section 7 summaries the results and possible future avenues for research.

2. Physical basis

In the hydrodynamic approximation, the evolution of the solar wind flow is governed by the equations of mass, momentum and energy conservation for a hydrodyanmic flow. We here follow the basic framework outlined in the 'pyro' python library of hydrodynamics examples (Harpole et al. 2019; Zingale 2014). However, we develop a solver fully integrated within the SURF framework, rather than produce a 'wrapper' for that existing codebase.

Ignoring gravity and viscous stress, we therefore seek to solve:

$$\text{Conservation of mass: } \frac{\partial \rho}{\partial t} + \nabla \cdot (\rho \mathbf{v}) = 0, \tag{1}$$

$$\text{Conservation of momentum: } \frac{\partial (\rho \mathbf{v})}{\partial t} + \nabla \cdot (\rho \mathbf{v}\mathbf{v}) + \nabla p = 0, \tag{2}$$

and

$$\text{Conservation of energy: } \frac{\partial (\rho E)}{\partial t} + \nabla \cdot (\mathbf{v} E) + \nabla \cdot (p \mathbf{v}) = 0, \tag{3}$$

where ρ is the mass density, $\mathbf{v}$ is the fluid velocity, p is the fluid pressure and E is the total fluid energy density, given by:

$$E = \frac{1}{2}\rho \mathbf{v}^2 + E_{INT}, \tag{4}$$

where E_{INT} is the internal energy density of the gas. For an ideal gas:

$$E_{INT} = \frac{p}{\gamma - 1}, \tag{5}$$

where γ is the polytropic index, taken to be 1.5.

Considering only the radial (r) direction in spherical geometry, $\mathbf{v}$ is simply the radial speed, v, and 1D Euler equation becomes:

$$\frac{\partial \mathbf{U}}{\partial t} + \frac{1}{r^2}\frac{\partial (r^2 \mathbf{F})}{\partial r} = \mathbf{S}, \tag{6}$$

where the conserved variables, $\mathbf{U}$, are:

$$\mathbf{U} = \begin{bmatrix} \rho \\ \rho v \\ \rho E \end{bmatrix}, \tag{7}$$

and the fluxes, $\mathbf{F}$, are:

$$\mathbf{F} = \begin{bmatrix} \rho v \\ \rho v^2 + p \\ v(E + p) \end{bmatrix}. \tag{8}$$

$\mathbf{S}$ is the geometric source vector. In Cartesian coordinates, $\mathbf{S} = 0$. However, in spherical coordinates, there is a geometric source of momentum arising from the fact that the surface area of a sphere grows as $1/r^2$. This results in a geometric pressure gradient. Therefore:

$$\mathbf{S} = \begin{bmatrix} 0 \\ \frac{2p}{r} \\ 0 \end{bmatrix}. \tag{9}$$

3. Numerical implementation

In order to solve the physical equations in Section 2, they are discretized in radial distance, r, and time, t, using a finite volume method. Thus a conserved variable at coordinates (r, t) becomes:

$$\mathbf{U}(r, t) \rightarrow \mathbf{U}_i^n = \mathbf{U}(r_i, t_n) \tag{10}$$

where r_i is the radial distance of the centre of the i^{th} grid cell, and t_n is the n^{th} time step. We solve on fixed, uniform radial grid, with grid cell spacings of Δr. We refer to the interface between cell i and $i + 1$ as $i + 1/2$. Time steps

are denoted by n, with spacing between consecutive time steps as Δt, which is variable to ensure stability (see discussion below). Note that the SURF-hydro output, however, is linearly interpolated onto a fixed, uniform time grid to ensure compatibility with the existing plotting and analysis codebase.

As each grid cell is part of a spherical shell, the area at each cell interface is $A_{i\pm1/2} = 4\pi r^2_{i\pm1/2}$. The evolution of a conserved quantity at grid cell i is then given by:

$$\frac{d\mathbf{U}}{dt} = \mathcal{L}(\mathbf{U}) \tag{11}$$

where $\mathcal{L}$ is the spatial discretization operator:

$$\mathcal{L}(\mathbf{U}) = -\frac{1}{V_i}\left(r^2_{i+1/2}\mathbf{F}_{i+1/2} - r^2_{i-1/2}\mathbf{F}_{i-1/2}\right) + \mathbf{S}_i \tag{12}$$

and V_i is the volume of the shell at distance r_i:

$$V_i = \frac{1}{3}(r^3_{i+1/2} - r^3_{i-1/2}). \tag{13}$$

As shown in Equation 9, the geometric source terms are zero for mass and energy. For momentum, however, spherical geometry results in a net component of the pressure force acting in the radial direction. Thus the source term is given by:

$$\mathbf{S_i} = \begin{bmatrix} 0 \\ p_i \frac{A_{i+1/2} - A_{i-1/2}}{v_i} \\ 0 \end{bmatrix} \tag{14}$$

In order to compute the fluxes through the inner and outer cell boundaries, we must first must compute $\mathbf{U}$ either side of the cell interfaces, rather than just the average values at the cell centres. Two reconstruction approaches are used. Like the original HUXt, one is a first order approach, the piecewise constant method (PCM). In PCM, the value either side of the interface is simply assumed to be the value at the cell centre. So at interface $i + 1/2$ – which is the outer boundary of cell i and inner boundary of cell $i+1$ – the state at the inner edge of the interface is given by $\mathbf{U_{INNER}} = \mathbf{U_i}$, while the outer edge is given by $\mathbf{U_{OUTER}} = \mathbf{U_{i+1}}$.

But the default method in SURF-hydro is to use a second-order solution, Piecewise Linear Method (PLM). This uses the linear gradient in $\mathbf{U}$, such that at the $i+1/2$ interface, $\mathbf{U_{INNER}} = \mathbf{U_{i+1/2}}\Delta\mathbf{U_i}$ and $\mathbf{U_{OUTER}} = \mathbf{U_{i+1}} - 1/2\Delta\mathbf{U}_{i+1}$. This retains sharper features, likes shocks, but requires a gradient limiter. We use the monotonized central limiter (Van Leer 1977) to prevent spurious oscillations while maintaining second-order accuracy away from extrema.

Next, for both reconstruction methods, we must solve for the discontinuities across cells. We use a Harten-Lax-van Leer-Contact (HLLC Toro 2009; Toro, Spruce, and Speares 1994) solver that assumes the solution consists of two waves (inner and outer) and a contact discontinuity in between. Either side of the contact discontinuity – and between the inner and outer call interfaces – are two

intermediate 'star states', $\mathbf{U_{*INNER}}$ and $\mathbf{U_{*OUTER}}$. The pressure and velocity are equal in these two regions, but the density and energy may be different. The HLLC solver evaluates the wave speeds and determines which region ($\mathbf{U_{i-1/2}}$, $\mathbf{U_{*INNER}}$, $\mathbf{U_{*OUTER}}$, $\mathbf{U_{i+1/2}}$) is sampled at the interface, then returns the corresponding flux.

The final step is the time update. For the PCM reconstruction, we use the 1st order forward Euler time integration, where:

$$\mathbf{U^{n+1}} = \mathbf{U^n} + \Delta t \mathcal{L}(\mathbf{U^n}) \tag{15}$$

For the PLM reconstruction, it is necessary to use the 2nd order Runge-Kutta method. Here we first compute the predictor state, which is the same as the 1st order solution:

$$\mathbf{U^p} = \mathbf{U^n} + \Delta t \mathcal{L}(\mathbf{U^n}) \tag{16}$$

and then to compute the 2nd order correction:

$$\mathbf{U^{n+1}} = \mathbf{U^n} + \frac{\Delta t}{2}\left[\mathcal{L}(\mathbf{U^n}) + \mathcal{L}(\mathbf{U^p})\right] \tag{17}$$

For both PCM and PCL, the time step must be chosen to meet the Courant-Friedrichs-Lewy (CFL) stability condition, such that:

$$\Delta t = C \min_i \left(\frac{\Delta r}{|v_i| + c_i} \right) \tag{18}$$

where $c_i = \sqrt{\gamma p_i / \rho_i}$ is the local sound speed and C is a constant to ensure stability. To balance computational efficiency and stability we use $C = 0.8$ for PCM and 0.6 for PLM.

As in HUXt, the user can specific the radial grid, with the time step being adjusted to match the associated CFL conditions. A default grid size of 1.5 solar radii (r_S) is used. Two- and three dimensional HUXt runs involve running a series of independent SURF-HUXt and SURF-hydro 1D models. Thus while longitudinal and latitudinal grid spacing can also be specified, this has no direct numerical or stability implications. By default, 128 longitudinal grid cells are used, and 45 latitudinal cells. All plots and analysis in this study use the default grids.

4. Validation

In order to test the numerical implementations of SURF-hydro described above, we compare with an analytical solution for a steady-state solar wind expansion in diverging spherical geometry. This differs from the classic Parker solar wind solution (Parker 1958) in that it ignores gravity and allows temperature to vary adiabatically.

This solution treats the solar wind acceleration as a one-dimensional isentropic flow through a nozzle with cross-sectional area $A(r) \propto r^2$. It can then be shown

(Anderson 2021) that the temperature, density and flow speed are given by: .

$$T(r) = T_0 \left[\frac{1 + \frac{\gamma-1}{2} M_0^2}{1 + \frac{\gamma-1}{2} M(r)^2} \right] \tag{19}$$

$$v(r) = v_0 \frac{M(r)}{M_0} \sqrt{\frac{T(r)}{T_0}} \tag{20}$$

$$\rho(r) = \rho_0 \frac{M_0}{M(r)} \sqrt{\frac{T_0}{T(r)}} \left(\frac{r_0}{r} \right)^2 \tag{21}$$

where $M(r) = v(r)/c(r)$ is the local Mach number.

This analytical solution exactly conserves mass flux ($\rho v r^2 = \text{const}$) and provides a benchmark for validating SURF-hydro in smooth, shock-free flows (Toro 2009).

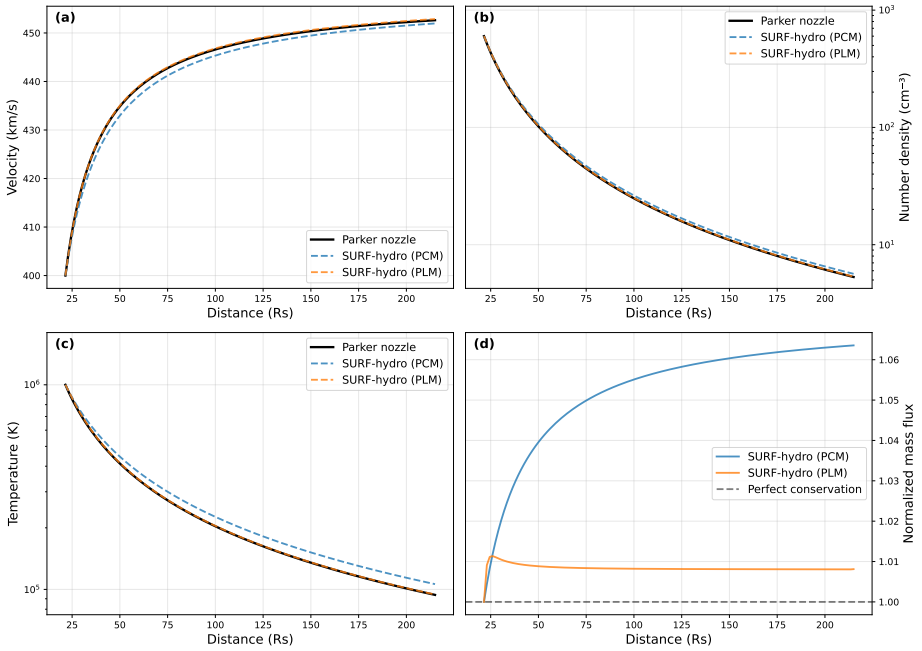

Figure 1. Comparison of SURF-hydro and analytical solar wind solutions from 0.1 to 1 AU (21.5 to 215 Rs). (a) Solar wind speed, v, as a function of heliocentric distance. The analytical solution is shown as a solid black line, with SURF-hydro PCM and PLM solutions shown as blue and orange dashed lines, respectively. (b) number density, n_P, assuming a proton plasma, (c) temperature, T (d) change in total mass, in the same format as (a).

Figure 1 shows comparisons of the SURF-hydro solutions with the analytical steady-state solar wind solution. All models use inner boundaries at 0.1 AU and inner boundary conditions of $v = 400$ km s^{-1}, T = 1 MK and a mass density computed from assuming a proton plasma of number density $n_P = 600$ cm^{-3}. For

the analytical model, these values result in 1 AU properties of $v = 453$ km s^{-1}, T = 94000 K and $n_P = 5$ cm^{-3}, which are fairly typical values (e.g. Owens 2020). For the SURF-hydro solutions, the model solutions are shown after the standard spin up of 5 days, to allow propagation of the inner boundary conditions through the whole 1-AU domain.

By eye, the SURF-hydro-PLM solution is nearly identical to the analytical benchmark solution. Over the whole domain, the error error in v is 0.04%, in n_P is 0.89%, and in T is 0.85%. For SURF-hydro-PCM, the deviation from the analytical benchmark solution is visible in the plots, particularly for temperature. Indeed, the error in v is 0.40%, in n_P is 5.63% and in T is 11.17%. Perhaps more important is the conservation of mass in the simulation. For SURF-hydro-PCM, the mass flux deviates from the inner boundary condition by 5.5% at 1 AU and is still continuing to gradually rise even at the outer boundary. This could be reduced by increasing the spatial and temporal resolution of HUXt, but that would come with additional computation cost and PCM would still have difficulty with capturing shocks. By contrast, the second-order scheme of SURF-hydro-PLM conserves mass to within 1%. Furthermore, even this small deviation is due entirely to the 2nd order scheme needing to interpolate across the inner boundary. Within the main computational domain, mass is conserved to machine accuracy.

For PCM, the 5-day run for a single longitude takes 0.03 seconds on a standard desktop CPU, while the PLM run takes 0.1 seconds. This compares with the original (incompressible) HUXt runtime of around 0.02 seconds. Thus the 2nd order solver does add significant – approximately x5 – computational overhead compared to HUXt, but SURF-hydro is still rapid enough for most of the original HUXt use cases. The PLM solver is used through the remainder of this paper. However, PCM is still included as an option within SURF for situations where large numbers of ambient solar wind solutions are required, and the computation time is important.

5. Ambient solar wind

The solar wind acceleration is prescribed as an analytical function in SURF-HUXt. This empirical relation is intended to mimic the spherical pressure gradient (Riley and Lionello 2011). For SURF-hydro, this process arises naturally, meaning solar wind acceleration is sensitive to the choice of temperature and (to a lesser extent) desnity at the inner boundary.

Figure 2 uses SURF-hydro to show how v at 1 AU varies for different T and n_P at 0.1 AU. A uniform v of 400 km s^{-1} is used throughout. Proton temperature at 0.1 AU has a strong effect on the resulting solar wind acceleration. A temperature of 1 MK at 0.1 AU produces about a 10% increase in solar wind speed by 1 AU, whilst a 3 MK corona results in around a third increase in speed. Conversely, solar wind density at 0.1 AU does not affect solar wind acceleration, despite contributing to the solar wind thermal pressure term. This is because the momentum is affected by pressure gradient with radius, which is unaffected by a change in the magnitude of the density. This is also evident from the Parker

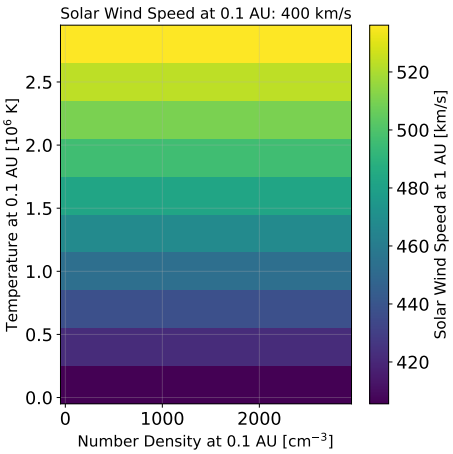

Figure 2. Solar wind speed at 1 AU for a range of proton density and temperatures at 0.1 AU. A constant solar wind speed at 0.1 AU of 400 km s^{-1} is used throughout.

nozzle solution too, wherein the solar wind speed at a given difference depends only on the initial temperature and initial speed, not the density. Note, however, that once there is structure in the solar wind speed at 0.1 AU, the density will begin to affect dynamics as it can result in radial pressure gradients. This is shown in Section 6.

It is therefore important to accurately determine not only speed at 0.1 AU, but also temperature, and – to a lesser extent – density. While full MHD solutions of the corona can in principle directly provide this information (Perri et al. 2023), in practice the coronal-model output used by solar wind models is typically limited to the radial magnetic field and radial flow speed (Linker et al. 2016; Riley, Linker, and Mikic 2001). Thus it is necessary to estimate n_P and T at the inner boundary on the basis of specified v. Typically some form of equilibrium is assumed at the solar wind model inner boundary. A range of approaches have been used; constant mass flux (Detman et al. 2006), constant kinetic energy flux (Odstrcil and Pizzo 1999; Pomoell and Poedts 2018) or constant momentum flux (Riley et al. 2011) are often invoked to infer n_P from v. Then constant thermal pressure is used to determine T. For use with interplanetary scintillation (IPS) derived solar wind speeds, there have been attempts to use purely empirical relations between n_P and T with v, which do not explicitly impose pressure balance (Hayashi, Tokumaru, and Fujiki 2016). However, these are typically applied much further out into the heliosphere ($\sim 50 - 60$ r_S), where most solar wind acceleration has already ceased (e.g. see Figure 1a). (Shiota et al. 2014) also used empirical relations derived from *Helios* observations to define n_P and T at the inner boundary, and produced reasonable speeds in near-Earth space. However, they did not consider the accuracy of density and temperature.

In general, there has not been systematic validation of these assumptions across a large dataset, largely due to the computational cost of such endeavours. It is also likely (see analysis below) that such approaches have been primarily

tuned to match solar wind speed in near-Earth space, rather then density and temperature.

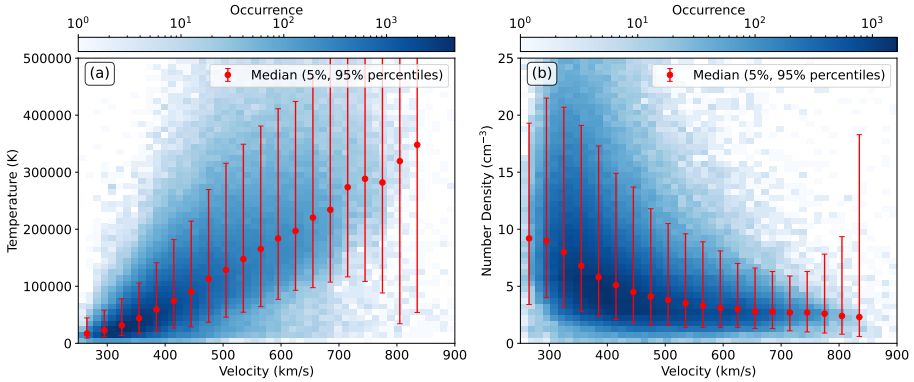

Figure 3. OMNI observations of solar wind parameters at 1 AU over the period 1995-2026 at 1-hour resolution. ICMEs have been removed. Panels show: (a) proton temperature, T, against proton radial velocity, v; (b) Proton number density, n_P, against v. The colour scale shows 2D histograms of occurrence on a log scale. The red dots show the median values in uniform v bins, with red lines spanning the 5- to 95 percentiles.

In future work, SURF-hydro will be used to assess the implications of all the equilibrium approaches over an extended time interval. Here, we demonstrate a simple non-equilibrium approach that performs well in reproducing solar wind speed, density and temperature at 1 AU.

Figure 3 shows an analysis of near-Earth solar wind data in order to characterise the relations of radial speed with density and temperature. Using OMNI data for the period of near-contiguous observations (1995 to 2026) at 1-hour resolution, we first remove all periods identified as interplanetary CMEs (ICMEs) using the updated list from Richardson and Cane (2010). Two dimensional occurrence histograms are shown in Figures 3a and b. The data are then binned in v and the median values of density and temperature computed. These are listed in Table 1. However, these are values at 1 AU, but we require relations between n_P, T and v at the SURF-hydro inner boundary radius (typically 0.1 AU).

Each set of v, n_P and T values at 1 AU is used with Equations 19 to 21 to compute the 0.1 AU equivalents. These are shown in Table 4. This is shown purely as a typical example. In practice, we use the relations at 1 AU (Table 1 to compute such look-up tables for the specific inner boundary distance specified for each SURF-hydro run, which varies for different observational input sources. Linear interpolation of this look-up table is used to compute n_P and T at the inner boundary. As with many of the boundary condition construction methods, these relations could be used with any solar wind model, not just the SURF models.

In order to demonstrate how well these empirical relations work, we produce an example solar wind forecast with SURF-hydro. OMNI near-Earth solar wind observations for 2019-8-18 to 2019-9-15 are used to construct v as a function of Carrington longitude at 0.1 AU, following the methodology of Owens et al.

Table 2. Table of median density and temperature for given solar wind speeds at 1 AU.

Velocity (km/s)	Number Density (cm^{-3})	Temperature (K)
265	9.20	1.72e+04
295	9.00	2.26e+04
325	8.00	3.13e+04
355	6.80	4.39e+04
385	5.80	5.91e+04
415	5.10	7.46e+04
445	4.50	9.05e+04
475	4.10	1.13e+05
505	3.80	1.29e+05
535	3.50	1.48e+05
565	3.30	1.65e+05
595	3.10	1.84e+05
625	3.00	1.97e+05
655	2.80	2.21e+05
685	2.80	2.34e+05
715	2.70	2.74e+05
745	2.70	2.88e+05
775	2.60	2.82e+05
805	2.40	3.19e+05
835	2.30	3.48e+05

(2026). Estimates of n_P and T at 0.1 AU are then derived from the empirical relations in Table 4.

The 0.1 AU boundary conditions shown in Figure 4 were then used to drive both SURF-HUXt and SURF-hydro forward in time for a further 27 days from 2019-9-10. The results are shown in Figure 5. (For clarity: Only solar wind speed observations from prior to the period shown in Figure 5 were used to make the forecast. And no density or temperature observations were used at all.)

The SURF forecast reproduces the general solar wind speed structure in near-Earth space very well, as the previous 27 days had also been similar. Of course, this is not always the case, as shown in **?**. This interval was specifically chosen as it is a representative example of recurrent solar wind wind and we here seek to determine how well density and temperature can be reconstructed when the large-scale solar wind speed structure is broadly correct. The results are extremely promising. The base-level proton number density of around 5 cm^{-3} is well captured, with stream interaction regions (SIRs) producing solar wind compressions and density spikes lasting 10s of hours with magnitudes of 10s cm^{-3}. There is a similar picture for temperature, with both observed and modelled proton temperature ranging from around 5×10^4 K in very slow wind, to 5×10^5 K in the compressed solar wind at stream interaction regions. For the major stream interaction region on 2019-9-27, SURF-hydro overestimates the

Table 4. The same as Table 1, but for properties mapped back to 0.1 AU using the relations in Equations 19 to 21.

Velocity (km/s)	Number Density (cm^{-3})	Temperature (K)
250	976.77	1.77e+05
277	959.39	2.33e+05
302	861.53	3.25e+05
325	743.37	4.59e+05
347	643.83	6.23e+05
370	572.32	7.91e+05
394	508.89	9.62e+05
414	470.71	1.21e+06
439	436.65	1.38e+06
464	403.84	1.59e+06
489	381.11	1.78e+06
515	358.12	1.98e+06
544	344.78	2.11e+06
568	322.86	2.37e+06
597	321.18	2.51e+06
615	313.72	2.95e+06
645	311.97	3.10e+06
682	295.26	3.01e+06
703	274.72	3.42e+06
728	263.84	3.73e+06

temperature and density magnitudes by around 50%, which may be due to the 1D nature of the solution; deflection of flow away from the radial is not possible.

However, it is important to put the scale of such errors into the wider context. The blue lines in Figure 5 show the Space Weather Prediction Center's (SWPC's) WSA-Enlil run for the same period (constructed from four separate 5-day forecasts, so the forecast lead time is generally much lower that the SURF runs). There is some evidence that the observed pattern in v is present in the WSA-Enlil solution, but the dynamic range is much reduced. There is almost no variation in n_P, while T is systematically an order of magnitude too low. Thus the SURF-hydro solution is providing much more accurate and useful information at this time. Of course, Enlil contains a much more accurate representation of solar wind physics physics than SURF-hydro. But the solution at 1-AU is primarily sensitive to the model boundary conditions (Heinemann et al. 2025), not the model physics.

Figure 6 investigates the importance of correctly specifying the 0.1 AU plasma conditions in more detail. All data are averaged to 1-hour and then binned by speed, density and temperature at 1 AU. Only parameter space containing at least 10 values is shown. The right hand panel shows 1 AU properties for SWPC runs of WSA-Enlil over the period 2019 through 2022. The centre panel shows the same analysis for the OMNI near-Earth solar wind observations, with periods identified as ICMEs by the Richardson and Cane (2010) catalogue removed.

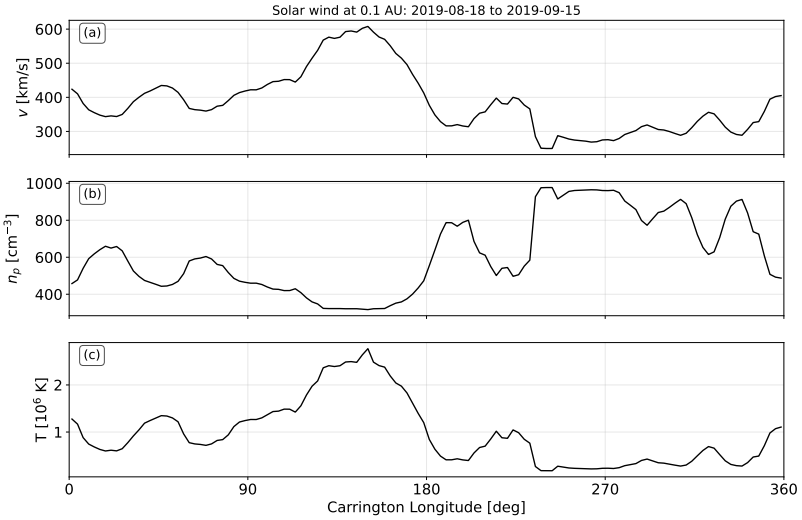

Figure 4. Solar wind properties at 0.1 AU as a function of Carrington longitude. (a) Solar wind speed at 0.1 AU, $v_{0.1\mathrm{AU}}$, generated by 'backmapping' near-Earth solar wind observations for the period 2019-8-18 to 2019-9-15, following the methodology of Owens et al. (2026). (b) Proton number density at 0.1 AU derived from $v_{0.1\mathrm{AU}}$ and the relations in Table 4 (c) Proton temperature at 0.1 AU, derived from $v_{0.1\mathrm{AU}}$ and the relations in Table 4

There are a number of notable differences. Firstly, the range of speeds in WSA-Enlil is reduced compared to observations. This could be a result of under-dispersed speeds in the WSA solution. The lack of variability in speed could then lead to the observed lack of varibaility in density too, as there is reduced opportunity to form strong stream interaction regions. However, it is clear that the problem is greater than that, as the WSA-Enlil temperatures are far too low, even allowinf for the reduced range of speeds produced by WSA-Enlil. This must be an issue with specifying the initial temperatures, suggesting that the equilibrium assumption employed in WSA-Enlil is incorrect.

The right-hand panel of Figure 6 shows the SURF-hydro solution, with initial speeds specified by backmapping the OMNI observed speeds. Thus the fact that SURF-hydro matches the range of speeds has been explicitly built into the reconstruction. What is important, however, is that the 0.1-AU densities and temperatures that are derived using the empirical relations in Table 4 then produce the correct range of densities and temperatures at 1 AU, with broadly the correct correlations. We therefore suggest that WSA-Enlil (and other coupled models) could likely be significantly improved by employing similar empirical density and temperature relations, rather than using equilibrium assumptions.

These examples only consider one point in the heliosphere; near-Earth space. The radial acceleration could still be systematically biassed. It is important to test against inner heliosphere observations, such as provided by *Parker Solar*

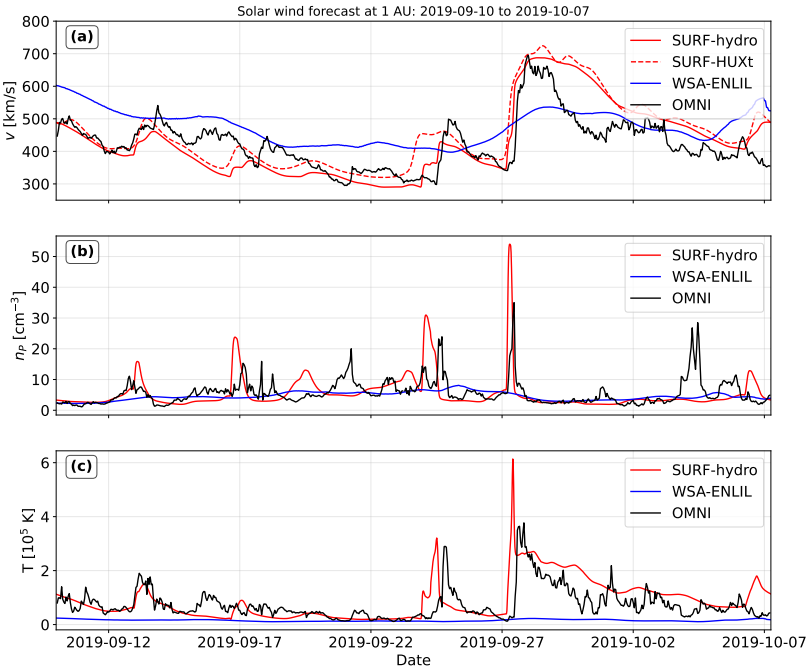

Figure 5. Solar wind forecasts made on on 2019-9-10 for the next 27 days using SURF and the input conditions shown in Figure 4. Black lines show OMNI observations, dashed red lines show SURF-HUXt, and solid red lines show SURF-hydro. (a) Solar wind speed at 1 AU, (b) proton number density at 1 AU, and (c) proton temperature at 1 AU. For comparison, a series of 5-day forecasts from the Space Weather Prediction Center's WSA-Enlil runs are shown in blue.

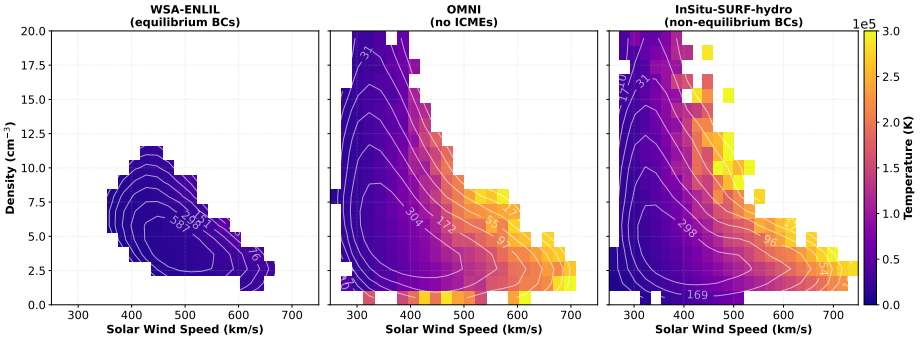

Figure 6. Solar wind conditions at 1 AU over the period 2019-2023 at 1-hour resolution for (left) WSA-Enlil, (centre) OMNI in situ observations, and (right) InSitu-SURF-hydro. Mean density is shown as a function of mean solar wind speed, with mean temperature indicated by the colourscale. Only points with at least 10 values are shown. The white contours show occurrence.

Probe and *Solar Orbiter*. This will provide a much stronger constraint on the solar wind acceleration (e.g. Badman et al. 2025).

6. Coronal mass ejections

Any space-weather modelling system needs to incorporate non-steady-state flows associated with coronal mass ejections (CMEs). The standard operational forecasting approach is to characterise the kinematics of CMEs – speed, direction, angular width – by fitting a simple geometric model to white-light coronagraph observations (Zhao, Plunkett, and Liu 2002). A perturbation at the solar wind model inner boundary is then introduced with the same basic properties (Odstrcil, Riley, and Zhao 2004). This localised and transient perturbation can be a simple speed perturbation, or also involve changes to the solar wind density and temperature at 0.1 AU. There has not been much systematic research into the exactly how these perturbations should be made. For example, the WSA-Enlil operational forecasting system used at US SWPC and the UK Met Office Space Weather Operations Centre (MOSWOC) insert a perturbation with the coronagraph-estimated CME speed, a typical ambient solar wind temperature at 0.1 AU and four times the ambient solar wind density at 0.1 AU (Zheng et al. 2013; Taktakishvili et al. 2009). Perturbation of these values is not something that something that is currently considered in ensemble forecasting (Mays et al. 2015), primarily because the parameter space is large and multiple runs 3DMHD models is computationally expensive. Very limited sensitivity analysis of these properties has been performed for a single event (Falkenberg et al. 2010), though this has primarily focussed further increasing the CME perturbation to be hotter and denser than the ambient solar wind conditions at 0.1 AU. The rationale behind this is that the cone-model representation of CMEs neglects their strong internal magnetic field, and thus increased thermal pressure is required to make up for the lack of magnetic pressure (see also Verbeke et al. 2022).

However, ICMEs at 1 AU are known to be very low proton density and proton temperature Richardson and Cane (2010). To demonstrate this, Figure 7 shows a super-posed epoch analysis of all magnetic clouds in the Richardson and Cane (2010) catalogue with an average speed greater than 500 km s^{-1}. We choose the fast events so that the sheath region ahead of the ICME can be included too. The median sheath duration for these events is 7.1 hours, while the median ICME duration is 26 hours. All event time series are normalised to these durations. For this 'typical' event, the sheath region is characterised by fast, dense and hot solar wind. The ICME body is characterised by a declining speed profile and lower density and temperature than the surrounding ambient solar wind. This density and temperature reduction partly arises from adiabatic expansion during transit from 0.1 to 1 AU. But there is also evidence that CMEs close to the Sun have already undergone significant expansion and cooling (Romeo et al. 2023; Davies et al. 2024). Therefore we do not rule out the possibility that CMEs should instead be represented as low density and temperature perturbations at 0.1 AU.

SURF-hydro is well suited to investigating this problem, as parameter space can be rapidly sampled. The magnetic pressure is neglected, but as discussed

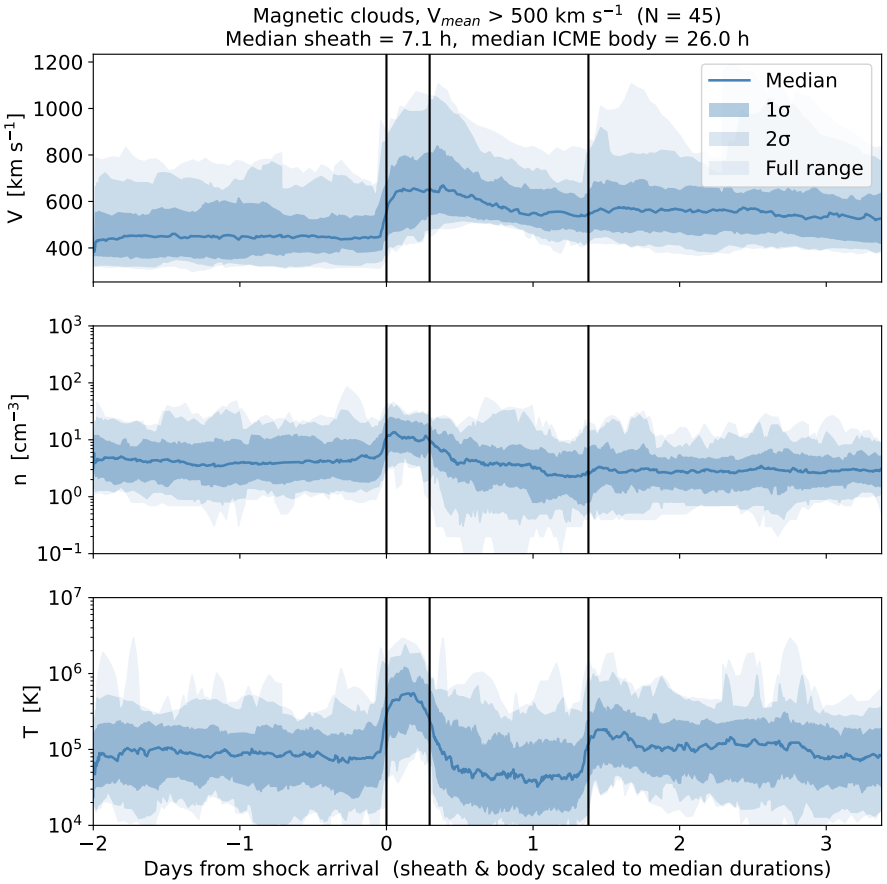

Figure 7. Super-posed epoch analysis of OMNI near-Earth solar wind data for all fast magnetic clouds between 1994 and 2025 (N = 45). Top: solar wind speed, middle: proton density, bottom: temperature. The median sheath duration for these events is 7.1 hours, and the median ICME body duration is 26 hours. All event durations have been normalised to these values to show typical variations. The vertical lines show the shock, ICME leading and trailing edges. The median value at each time is shown byt he blue line, with lighter shades showing 1-σ, 2-σ and the full range of values.

above, even in 3DMHD models CMEs are generally treated as hydrodynamic structures. Thus the core physics of adiabatic expansion and cooling is still well represented. Indeed, 1D hydrodynamic models have strong heritage in interpretation of CME dynamics and expansion (Gosling et al. 1998).

Figure 8 shows an example of typical CME solution in SURF-hydro. It uses a random WSA solution to provide v and B_R at 0.1 AU. Density and temperature at 0.1 AU are generated by interpolating the values in Table 4. These boundary conditions are used to generate a structured ambient solar wind that contains the heliospheric current sheet (HCS) within the slow wind. Heliospheric magnetic field (HMF) lines are traced as streak lines in the flow, and shown as black lines

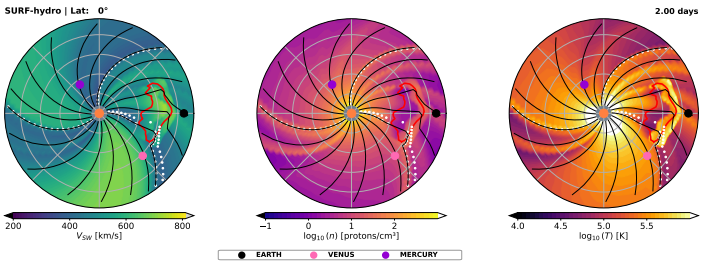

Figure 8. An example of the solar equatorial plane for a SURF-hydro solution for an arbitrary CME (directed at Earth, with angular width of 60° and speed 800 km s^{-1}) into a random WSA solar wind solution of v and B_R at 0.1 AU. Ambient desnity and temperature are determine from Table 4. The CME is represented by a v perturbation only; all other CME parameters are left at ambient values. Panels, from left to right, show snapshots of v, $\log_{10}(n_P)$ and $\log_{10}(T)$, respectively, 2 days after the CME launch. Red lines show the CME boundary, as determined by tracer particles. Black lines show streak lines of the flow, which approximate heliospheric magnetic field lines. White dots show the location of the heliospheric current sheet.

in all panels of Figure 8. Enhanced density and temperature fronts, aligned with the Parker spiral, are seen where fast wind meets slow (Pizzo 1991).

Into this ambient solar wind, a CME is inserted as a time-dependent speed perturbation at 0.1 AU, beginning at $t = 0$ and lasting for 12 hours (Owens et al. 2025). It has angular width of 60° and speed of 800 km s^{-1}. For this run, the density and temperature in the CME perturbation are left at ambient values. Tracer particles are inserted at 0.1 AU at the time that the CME leading and trailing edges pass the inner boundary. This results in the CME boundary shown as a red contour. It can be seen that there is hot, dense plasma ahead of the CME leading edge; this is the CME sheath region bounded by the shock front (Owens et al. 2005; Siscoe and Odstrcil 2008). This compression also propagates back into the CME body. The remainder of the CME body is cooler and less dense than the surrounding ambient wind, due to greater expansion.

Figure 9 shows the resulting time series at Earth, for both an ambient wind run of SURF-hydro (the black dashed lines) and with the CME present (the red solid lines). The vertical lines show the CME leading and trailing edges at Earth determined from the tracer particles. As seen from the snapshot, the interval of solar wind disturbed from the ambient values is greater in extent than the CME perturbation itself. The true time between the shock front and the CME leading edge is only a couple of hours, though if the CME leading edge were to be identified as the time when the density and temperature drops (Richardson and Cane 2010), it would be misidentified as more than twice that. This is in very close agreement with the observed typical sheath ahead of an ICME shown in Figure 7. The main body of the CME is indeed characterised by lower density and temperature than in the ambient wind, along with the characteristic declining velocity profile indicative of expansion in the radial direction (i.e., beyond the spherical expansion of the ambient solar wind). The CME trailing edge is more difficult to identify from these plasma signatures alone, and the CME trailing edge occurs before the return to ambient values. Both the true and apparent

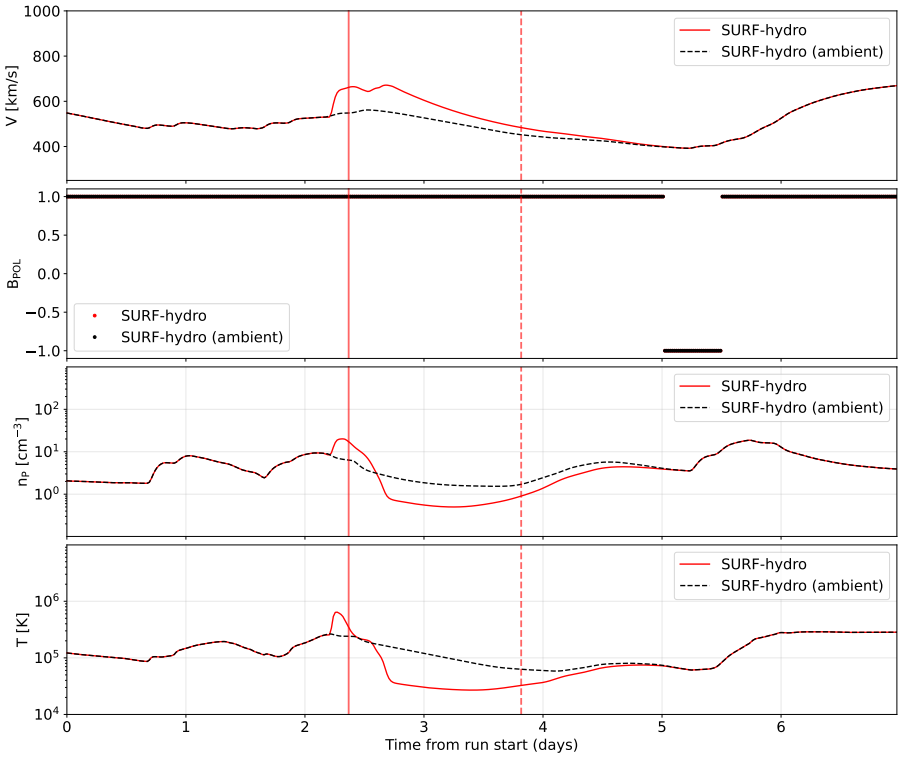

Figure 9. Time series of solar wind properties at Earth for the SURF-hydro solution shown in Figure 8. Red lines show the CME run, black dashed lines show the ambient run. Panels, from top to bottom, show v, $\mathrm{B_{POL}}$, $\mathrm{n_P}$ and T. Solid red vertical lines show the time of the CME leading edge, while vertical red dashed lines show the CME trailing edge.

CME durations are a little over 24 hours, in approximate agreement with typical observations (Richardson and Cane 2010, and Figure 7).

Figure 10 shows the kind of sensitivity analysis that is made more accessible by SURF-hydro. The two circular plots show solar wind speed in the solar equatorial plane for very similar SURF runs; the same ambient solar wind, the same CME speed, direction and angular width, but different initial CME densities and temperatures. The right-hand plot uses 0.1 AU CME values of $\mathrm{n_P} = 2000$ cm^{-3} and $T = 2.5 \times 10^6$ K, whereas the middle plot shows a CME with initial values of $\mathrm{n_P} = 500$ cm^{-3} and $T = 1 \times 10^6$ K. There are significant differences. The hot, dense CME arrives at Earth with a shorter transit time and a faster arrival speed, expands more to have greater radial extent and drives a stronger shock with a thicker sheath region.

The 2D colourmaps on the right investigate the effect of initial CME density and temperature on 1-AU transit time and 1-AU arrival speed for this specific ambient solar wind structure. In general, temperature decreases transit time and increases arrival speed, primarily owing to the increasing CME expansion. The relation with density is more complex. For higher temperatures, there is a weak

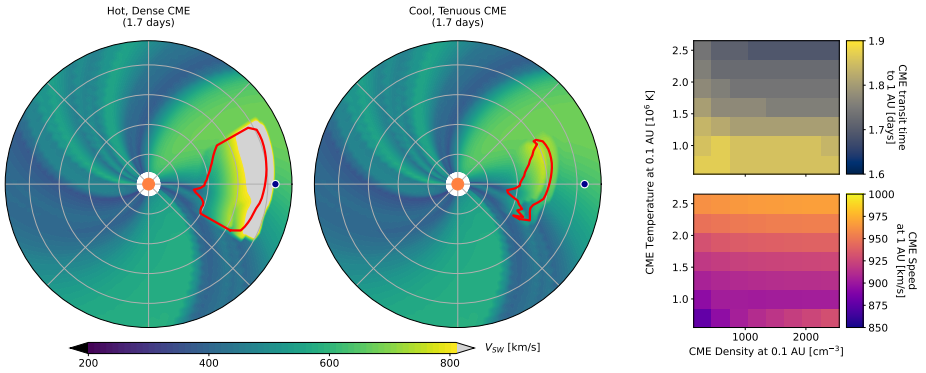

Figure 10. Left and centre: Two SURF-hydro runs after 1.7 days of the same ambient solar wind and with a CME with the same speed, direction and angular width, but different density and temperatures at 0.1 AU. Right: CME arrival time (top) and CME arrival speed (bottom) for a range of initial CME densities and temperatures.

negative correlation between transit time and density. This is less prevalent at lower density. Perhaps the key takeaway from this plot is that – for this ambient solar wind structure and CME speed – the 1-AU transit time and arrival speed can vary by around 15-20%, depending on the initial CME parameters.

7. Summary and discussion

In this study, we can outlined and tested a 1D, compressible hydrodynamic model of the solar wind. This builds on the previous 'HUXt' model that uses an incompressible assumption. In order to take of advantage of the considerable toolset built up around the HUXt model, we have repackaged the general framework as SURF; Space-weather Utilities for Research and Forecasting. HUXt and the new 'hydro' models are options within SURF. While hydro is not as computationally efficient as HUXt, it is still rapid enough for use in large ensembles and parametric studies, which can be used to inform and improve future 3DMHD modelling. For example, a single SURF-HUXt 1D run for 5 days – adequate to predict CME propagation to Earth – takes around 0.02 seconds on standard desktop CPU. The same run with SURF-hydro is around 0.1 seconds. This is still around $\times 10^4$ less computational resource than 3DMHD and being written in pure python, is much simpler to get up and running on standard computer.

One practical advantage to solving for density and temperature, rather than just the solar wind flow speed is that synthetic, is that it is possible to use SURF output to construct synthetic heliospheric imager observations (Eyles et al. 2009; Howard and DeForest 2012; Odstrcil et al. 2020) with relatively low computational overhead. This potentially enables more rigorous data assimilation of heliospheric imager data (Barnard et al. 2019, 2020, 2023) to improve solar wind reconstructions for both scientific and forecasting use.

Most coronal models provide radial speed and magnetic field as inner boundary conditions to solar wind models (e.g. Arge et al. 2003; Riley, Linker, and

Mikic 2001). Thus it is necessary to derive density and temperature from the provided speed. The standard method is to assume form form of equilibrium state at the 0.1 AU inner boundary surface; either constant mass, momentum or kinetic energy flux to determine density, then constant thermal pressure to determine temperature (Pomoell and Poedts 2018). SURF-hydro allows these assumptions to be rigorously tested, which will form the basis of a future study. Here, we have proposed a simple non-equilibrium method to determine inner boundary density and temperature. We use empirical relations derived using 30 years of near-Earth observations, then backmap relations (allowing for acceleration and expansion) to 0.1 AU. This non-equilibrium method is shown to produce sensible values at 1 AU and to perform favourably in comparison to state-of-the-art methods like WSA-Enlil (Zheng et al. 2013). This methodology could be easily applied to other solar wind models.

Properties of CMEs at 0.1 AU are even more uncertain than the ambient solar wind boundary conditions. CME speeds are routinely characterised by coronagraphs (though with unknown, but likely very large uncertainties) and used to define time-dependent boundary condition perturbations in solar wind models (Zhao, Plunkett, and Liu 2002). For operational forecasting, the CME perturbation is assumed to have x4 ambient solar wind density and the same temperature as ambient wind (Taktakishvili et al. 2009). This is in contrast to observations at 1 AU that find CMEs are cool and tenuous, though this is expected to result from in-transit adiabatic expansion (Richardson and Cane 2010). Again, computational limitations mean that these modelling choices have not been systematically explored, something that SURF-hydro can potentially provide in a future study. Here, we show that CME density and temperature can affect propagation time and arrival speed at Earth through a structured solar wind by around 15-20%. This will be different for different CME and ambient solar wind contexts and could be assessed with suitable perturbations during ensemble forecasting.

Acknowledgements This research made use of Astropy (Price-Whelan et al. 2018) and SunPy (Barnes et al. 2020) open source software packages for astronomy and solar physics. Figures for this article were made with Matplotlib (Hunter 2007).

Author Contribution Owens led the development and writing. Barnard led the code verification, curation and packaging.

Funding This work was part-funded by Science and Technology Facilities Council (STFC) grant number UKRI1207 and Natural Environment Research Council (NERC) grant number NE/Y001052/1.

Data Availability All data are packaged with the analysis code at the Github repository below.

Materials Availability N/A

Code Availability Github and Zenodo links provided on acceptance.

Declarations

Conflict of interest The authors declare that they have no conflicts of interest.

Bibliography

References

Anderson, J.D.: 2021, *Modern compressible flow : with historical perspective*, 4th ed., international student ed edn. McGraw-Hill Education. https://cir.nii.ac.jp/crid/1970586434882680605.

Arge, C.N., Odstrcil, D., Pizzo, V.J., Mayer, L.R.: 2003, Improved Method for Specifying Solar Wind Speed Near the Sun. *AIP Conference Proceedings* **679**, 190. DOI.

Badman, S.T., Stevens, M.L., Bale, S.D., Rivera, Y.J., Klein, K.G., Niembro, T., Chhiber, R., Rahmati, A., Whittlesey, P.L., Livi, R., Larson, D.E., Owen, C.J., Paulson, K.W., Horbury, T.S., Morris, J., O'Brien, H., Dakeyo, J.-B., Verniero, J.L., Martinovic, M., Pulupa, M., Fraschetti, F.: 2025, Multispacecraft Measurements of the Evolving Geometry of the Solar Alfvén Surface over Half a Solar Cycle. *The Astrophysical Journal Letters* **995**, L37. DOI. https://doi.org/10.3847/2041-8213/ae0e5c.

Baratashvili, T., Braileanu, B.P., Bacchini, F., Keppens, R., Poedts, S.: 2025, Icarus 3.0: Dynamic heliosphere modelling. *Astron. & Astrophys.* **694**, A306. DOI.

Barnard, L., Owens, M.: 2022, HUXt—An open source, computationally efficient reduced-physics solar wind model, written in Python. *Frontiers in Physics* **10**. DOI.

Barnard, L.A., Owens, M.J., Scott, C.J., Jones, S.R.: 2019, Extracting Inner-heliosphere Solar Wind Speed Information from Heliospheric Imager Observations. *Space Weather* **17**. DOI.

Barnard, L., Owens, M.J., Scott, C.J., de Koning, C.A.: 2020, Ensemble CME Modeling Constrained by Heliospheric Imager Observations. *AGU Advances* **1**, e2020AV000214. _eprint: https://onlinelibrary.wiley.com/doi/pdf/10.1029/2020AV000214. DOI.

Barnard, L., Owens, M., Scott, C., Lang, M., Lockwood, M.: 2023, SIR-HUXt—A Particle Filter Data Assimilation Scheme for CME Time-Elongation Profiles. *Space Weather* **21**, e2023SW003487. DOI.

Barnes, W.T., Bobra, M.G., Christe, S.D., Freij, N., Hayes, L.A., Ireland, J., Mumford, S., Perez-Suarez, D., Ryan, D.F., Shih, A.Y., Contributors), P.P., Chanda, P., Glogowski, K., Hewett, R., Hughitt, V.K., Hill, A., Hiware, K., Inglis, A., Kirk, M.S.F., Konge, S., Mason, J.P., Maloney, S.A., Murray, S.A., Panda, A., Park, J., Pereira, T.M.D., Reardon, K., Savage, S., Sipőcz, B.M., Stansby, D., Jain, Y., Taylor, G., Yadav, T., Rajul, Dang, T.K., Contributors), S.: 2020, The SunPy Project: Open Source Development and Status of the Version 1.0 Core Package. *The Astrophysical Journal* **890**, 68. DOI. https://doi.org/10.3847/1538-4357/ab4f7a.

Bunting, K.A., Barnard, L., Owens, M.J., Morgan, H.: 2024, Constraints on Solar Wind Density and Velocity Based on Coronal Tomography and Parker Solar Probe Measurements. *Astrophys. J.* **961**, 64. DOI.

Davies, E.E., Rüdisser, H.T., Amerstorfer, U.V., Möstl, C., Bauer, M., Weiler, E., Amerstorfer, T., Majumdar, S., Hess, P., Weiss, A.J., Reiss, M.A., Green, L.M., Long, D.M., Nieves-Chinchilla, T., Trotta, D., Horbury, T.S., O'Brien, H., Fauchon-Jones, E., Morris, J., Owen, C.J., Bale, S.D., Kasper, J.C.: 2024, Flux Rope Modeling of the 2022 September 5 Coronal Mass Ejection Observed by Parker Solar Probe and Solar Orbiter from 0.07 to 0.69 au. *Astrophys. J.* **973**, 51. DOI.

Detman, T., Smith, Z., Dryer, M., Fry, C.D., Arge, C.N., Pizzo, V.: 2006, A hybrid heliospheric modeling system: Background solar wind. *J. Geophys. Res.* **111**, 7102. DOI.

Eyles, C.J., Harrison, R.A., Davis, C.J., Waltham, N.R., Shaughnessy, B.M., Mapson-Menard, H.C.A., Bewsher, D., Crothers, S.R., Davies, J.A., Simnett, G.M.: 2009, The heliospheric imagers onboard the STEREO mission. *Solar Phys.* **254**, 387. DOI.

Falkenberg, T.V., Vršnak, B., Taktakishvili, A., Odstrcil, D., MacNeice, P., Hesse, M.: 2010, Investigations of the sensitivity of a coronal mass ejection model (ENLIL) to solar input parameters. *Space Weather* **8**. _eprint: https://agupubs.onlinelibrary.wiley.com/doi/pdf/10.1029/2009SW000555. DOI.

Gosling, J.T., Riley, P., McComas, D.J., Pizzo, V.J.: 1998, Overexpanding coronal mass ejections at high heliographic latitudes: Observations and simulations. *J. Geophys. Res.* **103**, 1941. DOI.

Harpole, A., Zingale, M., Hawke, I., Chegini, T.: 2019, pyro: a framework for hydrodynamics explorations and prototyping. *Journal of Open Source Software* **4**, 1265. DOI.

Hayashi, K., Tokumaru, M., Fujiki, K.: 2016, MHD-IPS analysis of relationship among solar wind density, temperature, and flow speed. *J. Geophys. Res.* **121**, 7367. DOI.

Heinemann, S.G., Pomoell, J., Caplan, R.M., Owens, M.J., Jones, S., Upton, L., Jha, B.K., Arge, C.N.: 2025, Quantifying Uncertainties in Solar Wind Forecasting due to Incomplete Solar Magnetic Field Information. *Astrophys. J.* **986**, 166. DOI.

Hinterreiter, J., Amerstorfer, T., Temmer, M., Reiss, M.A., Weiss, A.J., Möstl, C., Barnard, L.A., Pomoell, J., Bauer, M., Amerstorfer, U.V.: 2021, Drag-Based CME Modeling With Heliospheric Images Incorporating Frontal Deformation: ELEvoHI 2.0. *Space Weather* **19**, e2021SW002836. DOI.

Howard, T.A., DeForest, C.E.: 2012, THE THOMSON SURFACE. I. REALITY AND MYTH. *The Astrophysical Journal* **752**, 130. DOI. https://doi.org/10.1088/0004-637X/752/2/130.

Hunter, J.D.: 2007, Matplotlib: A 2D Graphics Environment. *Computing in Science & Engineering* **9**, 90. DOI.

Lang, M., Owens, M.J.: 2019, A Variational Approach to Data Assimilation in the Solar Wind. *Space Weather* **17**, 59. DOI.

Linker, J., Mikic, Z., Biesecker, D.A., Forsyth, R.J., Gibson, W.E., Lazarus, A.J., Lecinski, A., Riley, P., Szabo, A., Thompson, B.J.: 1999, Magnetohydrodynamic modeling of the solar corona during whole sun month. *J. Geophys. Res.* **104**, 9809. DOI.

Linker, J.A., Caplan, R.M., Downs, C., Lionello, R., Riley, P., Mikic, Z., Henney, C.J., Arge, C.N., Kim, T., Pogorelov, N.: 2016, An Empirically Driven Time-Dependent Model of the Solar Wind. *Journal of Physics: Conference Series* **719**, 012012. DOI.

Mays, M.L., Taktakishvili, A., Pulkkinen, A., MacNeice, P.J., Rastätter, L., Odstrcil, D., Jian, L.K., Richardson, I.G., LaSota, J.A., Zheng, Y., Kuznetsova, M.M.: 2015, Ensemble Modeling of CMEs Using the WSA–ENLIL+Cone Model. *Solar Phys.* **290**, 1775. DOI.

Merkin, V.G., Lyon, J.G., Lario, D., Arge, C.N., Henney, C.J.: 2016, Time-dependent magnetohydrodynamic simulations of the inner heliosphere. *J. Geophys. Res.* **121**, 2866. DOI.

Odstrcil, D., Pizzo, V.J.: 1999, Three-dimensional propagation of coronal mass ejections (CMEs) in a structured solar wind flow: 1. CME launched within the streamer belt. *J. Geophys. Res.* **104**, 483.

Odstrcil, D., Riley, P., Zhao, X.-P.: 2004, Numerical simulation of the 12 May 1997 interplanetary CME event. *J. Geophys. Res.* **109**. DOI.

Odstrcil, D., Mays, M.L., Hess, P., Jones, S.I., Henney, C.J., Arge, C.N.: 2020, Operational Modeling of Heliospheric Space Weather for the Parker Solar Probe. *Astrophys. J. Supp.* **246**, 73. DOI.

Owens, M.: 2020, Solar-Wind Structure. *Oxford Research Encyclopedia of Physics*. DOI.

Owens, M.J., Cargill, P.J.: 2004, Non-radial solar wind flows induced by the motion of interplanetary coronal mass ejections. *Ann. Geophys.* **22**, 4397. DOI.

Owens, M.J., Riley, P.: 2017, Probabilistic Solar Wind Forecasting Using Large Ensembles of Near-Sun Conditions With a Simple One-Dimensional "Upwind" Scheme. *Space Weather* **15**, 1461. DOI.

Owens, M.J., Barnard, L., Arge, C.N.: 2024, The importance of boundary evolution for solar-wind modelling. *Sci. Rep.* **14**, 28975. DOI.

Owens, M.J., Lockwood, M., Barnard, L.A.: 2017, Coronal mass ejections are not coherent magnetohydrodynamic structures. *Scientific Rep.* **7**, 4152. DOI.

Owens, M.J., Cargill, P.J., Pagel, C., Siscoe, G.L., Crooker, N.U.: 2005, Characteristic magnetic field and speed properties of interplanetary coronal mass ejections and their sheath regions. *J. Geophys. Res.* **110**, 1. DOI.

Owens, M.J., Lang, M., Barnard, L., Riley, P., Ben-Nun, M., Scott, C.J., Lockwood, M., Reiss, M.A., Arge, C.N., Gonzi, S.: 2020, A Computationally Efficient, Time-Dependent Model of the Solar Wind for Use as a Surrogate to Three-Dimensional Numerical Magnetohydrodynamic Simulations. *Solar Phys.* **295**, 43. DOI.

Owens, M.J., Barnard, L.A., Verbeke, C., McGinness, B.P.S., Turner, H., Chi, Y., Gyeltshen, D., Lockwood, M.: 2025, Implications of Using Spheroidal "Cone Model" CMEs in Solar-Wind Models. *Space Weather* **23**, e2025SW004397. DOI.

Owens, M.J., Barnard, L.A., Turner, H., Gyeltshen, D., Edward-Inatimi, N., O'Donoghue, J., Lockwood, M., Watson, S., Rutala, M., Jackman, C.M., Riley, P.: 2026, Driving Dynamical Inner-Heliosphere Models With In Situ Solar Wind Observations. *Space Weather* **24**, e2025SW004675. DOI.

O'Donoghue, J., Moore, L., Melin, H., Stallard, T., Kurth, W.S., Owens, M., Bhakyapaibul, T., Tao, C., Connerney, J.E.P., Knowles, K.L., Kita, H., Roberts, K., Tiranti, P.I., Agiwal, O., Johnson, R., Wang, R., Thomas, E., Murakami, G.: 2025, Sub-Auroral Heating at Jupiter Following a Solar Wind Compression. *Geophys. Res. Lett.* **52**, e2024GL113751. DOI.

Parker, E.N.: 1958, Dynamics of the interplanetary gas and magnetic fields. *Astrophys. J.* **128**, 664. DOI.

Perri, B., Kuźma, B., Brchnelova, M., Baratashvili, T., Zhang, F., Leitner, P., Lani, A., Poedts, S.: 2023, COCONUT, a Novel Fast-converging MHD Model for Solar Corona Simulations. II. Assessing the Impact of the Input Magnetic Map on Space-weather Forecasting at Minimum of Activity. *Astrophys. J.* **943**, 124. DOI.

Pizzo, V.J.: 1991, The evolution of corotating stream fronts near the ecliptic plane in the inner solar system. II - Three-dimensional tilted-dipole fronts. *J. Geophys. Res.* **96**, 5405. DOI.

Pomoell, J., Poedts, S.: 2018, EUHFORIA: European heliospheric forecasting information asset. *J. Space Weather Space Clim.* **8**, A35. DOI.

Price-Whelan, A.M., Sipőcz, B.M., Günther, H.M., Lim, P.L., Crawford, S.M., Conseil, S., Shupe, D.L., Craig, M.W., Dencheva, N., Ginsburg, A., VanderPlas, J.T., Bradley, L.D., Pérez-Suárez, D., de Val-Borro, M., Contributors), P.P., Aldcroft, T.L., Cruz, K.L., Robitaille, T.P., Tollerud, E.J., Committee), A.C., Ardelean, C., Babej, T., Bach, Y.P., Bachetti, M., Bakanov, A.V., Bamford, S.P., Barentsen, G., Barmby, P., Baumbach, A., Berry, K.L., Biscani, F., Boquien, M., Bostroem, K.A., Bouma, L.G., Brammer, G.B., Bray, E.M., Breytenbach, H., Buddelmeijer, H., Burke, D.J., Calderone, G., Rodríguez, J.L.C., Cara, M., Cardoso, J.V.M., Cheedella, S., Copin, Y., Corrales, L., Crichton, D., D'Avella, D., Deil, C., Depagne, E., Dietrich, J.P., Donath, A., Droettboom, M., Earl, N., Erben, T., Fabbro, S., Ferreira, L.A., Finethy, T., Fox, R.T., Garrison, L.H., Gibbons, S.L.J., Goldstein, D.A., Gommers, R., Greco, J.P., Greenfield, P., Groener, A.M., Grollier, F., Hagen, A., Hirst, P., Homeier, D., Horton, A.J., Hosseinzadeh, G., Hu, L., Hunkeler, J.S., Ivezic, Z., Jain, A., Jenness, T., Kanarek, G., Kendrew, S., Kern, N.S., Kerzendorf, W.E., Khvalko, A., King, J., Kirkby, D., Kulkarni, A.M., Kumar, A., Lee, A., Lenz, D., Littlefair, S.P., Ma, Z., Macleod, D.M., Mastropietro, M., McCully, C., Montagnac, S., Morris, B.M., Mueller, M., Mumford, S.J., Muna, D., Murphy, N.A., Nelson, S., Nguyen, G.H., Ninan, J.P., Nöthe, M., Ogaz, S., Oh, S., Parejko, J.K., Parley, N., Pascual, S., Patil, R., Patil, A.A., Plunkett, A.L., Prochaska, J.X., Rastogi, T., Janga, V.R., Sabater, J., Sakurikar, P., Seifert, M., Sherbert, L.E., Sherwood-Taylor, H., Shih, A.Y., Sick, J., Silbiger, M.T., Singanamalla, S., Singer, L.P., Sladen, P.H., Sooley, K.A., Sornarajah, S., Streicher, O., Teuben, P., Thomas, S.W., Tremblay, G.R., Turner, J.E.H., Terrón, V., Kerkwijk, M.H.v., de la Vega, A., Watkins, L.L., Weaver, B.A., Whitmore, J.B., Woillez, J., Zabalza, V., Contributors), A.: 2018, The Astropy Project: Building an Open-science Project and Status of the v2.0 Core Package*. *Astrophys. J.* **156**, 123. DOI.

Richardson, I.G., Cane, H.V.: 2010, Near-Earth Interplanetary Coronal Mass Ejections During Solar Cycle 23 (1996 – 2009): Catalog and Summary of Properties. *Solar Phys.* **264**, 189. DOI.

Riley, P., Lionello, R.: 2011, Mapping Solar Wind Streams from the Sun to 1 AU: A Comparison of Techniques. *Solar Phys.* **270**, 575. DOI.

Riley, P., Linker, J.A., Mikic, Z.: 2001, An empirically-driven global MHD model of the solar corona and inner heliosphere. *J. Geophys. Res.* **106**, 15889. DOI.

Riley, P., Lionello, R., Linker, J.A., Mikic, Z., Luhmann, J., Wijaya, J.: 2011, Global MHD Modeling of the Solar Corona and Inner Heliosphere for the Whole Heliosphere Interval. *Solar Physics* **274**, 361. DOI. https://doi.org/10.1007/s11207-010-9698-x.

Romeo, O.M., Braga, C.R., Badman, S.T., Larson, D.E., Stevens, M.L., Huang, J., Phan, T., Rahmati, A., Livi, R., Alnussirat, S.T., Whittlesey, P.L., Szabo, A., Klein, K.G., Niembro-Hernandez, T., Paulson, K., Verniero, J.L., Lario, D., Raouafi, N.E., Ervin, T., Kasper, J., Pulupa, M., Bale, S.D., Linton, M.G.: 2023, Near-Sun In Situ and Remote-sensing Observations of a Coronal Mass Ejection and its Effect on the Heliospheric Current Sheet. *Astrophys. J.* **954**, 168. DOI.

Scherer, K., Marsch, E., Schwenn, R., Rosenbauer, H.: 2001, Long-term variations of the flow direction and angular momentum of the solar wind observed by Helios. *Astronomy & Astrophysics* **366**, 331. DOI.

Shiota, D., Kataoka, R.: 2016, Magnetohydrodynamic simulation of interplanetary propagation of multiple coronal mass ejections with internal magnetic flux rope (SUSANOO-CME). *Space Weather* **14**, 56. DOI.

Shiota, D., Kataoka, R., Miyoshi, Y., Hara, T., Tao, C., Masunaga, K., Futaana, Y., Terada, N.: 2014, Inner heliosphere MHD modeling system applicable to space weather forecasting for the other planets. *Space Weather* **12**, 187. DOI.

Siscoe, G., Odstrcil, D.: 2008, Ways in which ICME sheaths differ from magnetosheaths. *J. Geophys. Res.* **113**, A00B07. DOI. http://10.0.4.5/2008JA013142.

Taktakishvili, A., Kuznetsova, M., MacNeice, P., Hesse, M., Rastätter, L., Pulkkinen, A., Chulaki, A., Odstrcil, D.: 2009, Validation of the coronal mass ejection predictions at the Earth orbit estimated by ENLIL heliosphere cone model. *Space Weather* **7**. _eprint: https://agupubs.onlinelibrary.wiley.com/doi/pdf/10.1029/2008SW000448. DOI.

Toro, E.F.: 2009, *Riemann Solvers and Numerical Methods for Fluid Dynamics: A Practical Introduction*, Springer, Berlin, Heidelberg. ISBN 978-3-540-25202-3 978-3-540-49834-6. DOI. https://link.springer.com/10.1007/b79761.

Toro, E.F., Spruce, M., Speares, W.: 1994, Restoration of the contact surface in the HLL-Riemann solver. *Shock Waves* **4**, 25. DOI. https://doi.org/10.1007/BF01414629.

Toth, G., Sokolov, I.V., Gombosi, T.I., Chesney, D.R., Clauer, C.R., De Zeeuw, D.L., Hansen, K.C., Kane, K.J., Manchester, W.B., Oehmke, R.C., Powell, K.G., Ridley, A.J., Roussev, I.I., Stout, Q.F., Volberg, O., Wolf, R.A., Sazykin, S., Chan, A., Yu, B., Kóta, J.: 2005, Space Weather Modeling Framework: A new tool for the space science community. *J. Geophys. Res.* **110**, A12226. DOI.

Van Leer, B.: 1977, Towards the ultimate conservative difference scheme III. Upstream-centered finite-difference schemes for ideal compressible flow. *J. Comp. Phys.* **23**, 263. DOI.

Verbeke, C., Schmieder, B., Démoulin, P., Dasso, S., Grison, B., Samara, E., Scolini, C., Poedts, S.: 2022, Over-expansion of coronal mass ejections modelled using 3D MHD EUHFORIA simulations. *Adv. Space Res.* **70**, 1663. DOI.

Watson, S., Scott, C., Owens, M., Barnard, L., Lang, M.: 2025, Statistical Analysis of Comet Disconnection Events Using STEREO HI and a Data-assimilative Solar Wind Model. *Astrophys. J.* **982**, 66. DOI.

Zhao, X.-P., Plunkett, S.P., Liu, W.: 2002, Determination of geometrical and kinematical properties of halo coronal mass ejections using the cone model. *J. Geophys. Res.* **107**. DOI.

Zheng, Y., Macneice, P., Odstrcil, D., Mays, M.L., Rastaetter, L., Pulkkinen, A., Taktakishvili, A., Hesse, M., Masha Kuznetsova, M., Lee, H., Chulaki, A.: 2013, Forecasting propagation and evolution of CMEs in an operational setting: What has been learned. *Space Weather* **11**, 557. DOI.

Zingale, M.: 2014, pyro: A teaching code for computational astrophysical hydrodynamics. *Astronomy and Computing* **6**, 52. DOI.